

# IRAM-30m large scale survey of $^{12}\text{CO}(2-1)$ and $^{13}\text{CO}(2-1)$ emission in the Orion molecular cloud

O. Berné<sup>1,2,3</sup> N. Marcelino<sup>4</sup> J. Cernicharo<sup>1</sup>

olivier.berne@irap.omp.eu

Received \_\_\_\_\_; accepted \_\_\_\_\_

---

<sup>1</sup>Centro de Astrobiología (CSIC/INTA), Ctra. de Torrejn a Ajalvir, km 4, 28850, Torrejn de Ardoz, Madrid, Spain

<sup>2</sup>Université de Toulouse; UPS-OMP; IRAP; Toulouse, France

<sup>3</sup>CNRS; IRAP; 9 Av. colonel Roche, BP 44346, F-31028 Toulouse cedex 4, France

<sup>4</sup>NRAO, 520 Edgemont Road, Charlottesville, VA 22902, USA

## ABSTRACT

Using the IRAM 30m telescope we have surveyed a  $1 \times 0.8^\circ$  part of the Orion molecular cloud in the  $^{12}\text{CO}$  and  $^{13}\text{CO}$  (2-1) lines with a maximal spatial resolution of  $\sim 11''$  and spectral resolution of  $\sim 0.4 \text{ km s}^{-1}$ . The cloud appears filamentary, clumpy and with a complex kinematical structure. We derive an estimated mass of the cloud of  $7700 \text{ M}_\odot$  (half of which is found in regions with visual extinctions  $A_V$  below  $\sim 10$ ) and a dynamical age for the nebula of the order of  $0.2 \text{ Myrs}$ . The energy balance suggests that magnetic fields play an important role in supporting the cloud, at large and small scales. According to our analysis, the turbulent kinetic energy in the molecular gas due to outflows is comparable to turbulent kinetic energy resulting from the interaction of the cloud with the HII region. This latter feedback appears negative, i.e. the triggering of star formation by the HII region is inefficient in Orion. The reduced data as well as additional products such as the column density map are made available online<sup>1</sup>.

*Subject headings:* ISM: lines and bands — ISM: molecules — infrared: ISM

---

<sup>1</sup> [http://userpages.irap.omp.eu/~oberne/Olivier\\_Berne/Data](http://userpages.irap.omp.eu/~oberne/Olivier_Berne/Data)

## 1. Introduction

The structure and dynamical properties of the interstellar medium in galaxies is deeply influenced by the feedback of massive stars. Their ionizing photons (extreme UV,  $E > 13.6$  eV) generate HII regions, which expand rapidly within their parental molecular cloud. This expansion compresses molecular clouds and can trigger their gravitational collapse towards the formation of a new generation of low mass stars (Elmegreen 1998; Deharveng et al. 2010a). The interaction of the HII region with the surrounding cloud is also a source of hydrodynamical instabilities (Spitzer 1954; Frieman 1954; Berné et al. 2010), turbulence (Elmegreen & Scalo 2004) and chemical mixing (Roy & Kunth 1995; Berné & Matsumoto 2012) in the interstellar medium. In addition, outflows from young stellar objects can also inject kinetic energy in their parent molecular cloud (Bachiller 1996).

Given its proximity to us (414 pc, Menten et al. 2007), the Orion nebula is one of the most studied regions of massive star formation (see e.g. Genzel & Stutzki 1989; Bally 2008; Muench et al. 2008 for reviews). Traditionally, the “Orion nebula” refers to the visible part of the region, the HII region, powered by the ionizing radiation of the Trapezium OB association. It is part of a much larger complex, refereed to as the Orion molecular cloud (OMC), itself lying at the border of the Eridanis super bubble. Numerous studies have focused on specific objects in the Orion Nebula, such as the famous Proplyds, the Orion Kleinmann-Low (KL) Nebula, or the Orion bar. Studies of the large scale structure of the nebula are however sparse, because of the difficulty to obtain observations covering large areas of the sky with sufficient angular resolution, and because the interpretation of such datasets is challenging. Bally et al. (1987) reported  $^{13}\text{CO}$  observation of the entire Orion molecular cloud, including the Nebula, with a resolution of  $1'$  (Fig. 1). This study was the first to reveal the filamentary structure of the cloud. The Orion Nebula was found to lie at the center of an “integral shaped filament” (ISF) of molecular gas, itself part of a larger

filamentary structure extending from North to South over  $4^\circ$  (referred to as Orion A, see Bally et al. 1987 and Fig. 1). Several studies have investigated the degree scale properties of the nebula in various molecular tracers. Using  $^{12}\text{CO}$ ,  $^{13}\text{CO}$  and  $\text{C}^{18}\text{O}$  observations, Castets et al. (1990) provided a column density and an  $\text{H}_2$  density map of the ISF with an angular resolution of the order of  $100''$ . Using  $\text{C}^{18}\text{O}$  observations, Dutrey et al. (1991) identified clumps inside filaments distributed periodically, suggestive of externally triggered cloud collapse and fragmentation. Recently, Buckle et al. (2012) obtained a new survey in  $\text{CO}(3-2)$  along the ISF with a  $15''$  resolution (see their field of view in Fig. 1). Their study concluded that the cloud is magnetically supported and wrapped in a helical magnetic field. Shimajiri et al. (2011) recently reported a survey of the Orion molecular cloud in  $\text{CO}(1-0)$  with a spatial resolution of  $20''$  and a spectral resolution of  $1 \text{ km s}^{-1}$ . Using this dataset, the authors suggest that the formation of some clumps or protostars might have been triggered by the pressure exerted by the HII region (Shimajiri et al. 2011). The ISF was observed by Johnstone & Bally (1999) in the submillimeter continuum. These authors found a strong correlation between the CO and cold dust continuum emission. They also reported the presence of young stellar objects and pre-stellar clumps, mainly found in the northern part of the ISF. Spitzer observation have shown further evidence for this ongoing low mass star formation (Megeath et al. 2012). The HII region observed at large scales with VLA at 330 MHz by Subrahmanyan et al. (2001) shows a shell-like structure, suggesting high pressures exerted on the Northern cloud, while the gas is escaping in the South toward the general interstellar medium through cavities in the molecular gas. A similar idea was pointed out by Güdel et al. (2008) who have discovered the presence of an X-ray emitting plasma in thermodynamic equilibrium with the HII gas. Finally, the Veil of neutral gas situated in the foreground of the Orion nebula was recently mapped at high angular and spectral resolution by van der Werf et al. (2013), and seemingly confirms this idea that the HII region is in blister phase.

In this paper we present new observation of the  $^{12}\text{CO}$  and  $^{13}\text{CO}$  (2-1) rotational line at 1.3 mm observed with the IRAM 30m telescope in Granada. This dataset has an unprecedented spatial ( $\sim 11''$ ) and spectral ( $\sim 0.4 \text{ km s}^{-1}$ ) resolution, together with a large field of view ( $1 \times 0.8^\circ$ ). This data is available at [http://userpages.irap.omp.eu/~oberne/Olivier\\_Berne/Data](http://userpages.irap.omp.eu/~oberne/Olivier_Berne/Data).

## 2. Observations and data reduction

The observations were conducted at the IRAM 30m telescope in Granada, Spain, in March, April and October 2008. The data were obtained with the HERA receiver array, each polarization tuned to  $^{12}\text{CO}$  and  $^{13}\text{CO}$  lines (230.5 and 220.4 GHz respectively) with a spatial beamwidth of  $11''$ , and main beam efficiencies of 0.524 and 0.545 for  $^{12}\text{CO}$  and  $^{13}\text{CO}$  respectively. We used the versatile spectrometer VESPA as a backend providing 320 kHz of spectral resolution, ( $0.4 \text{ km s}^{-1}$ ). We observed using the On-The-Fly (OTF) mapping mode, with  $5''$  of data sampling in right ascension, and with steps of  $12''$  in declination. Since the beam of the telescope is  $\sim 11''$ , this implies that the resolution is equal to the telescope beam in right ascension, but is a factor of two larger in declination. Intensity calibration was performed every 3-4min using two absorbers at different temperatures, resulting in system temperatures between 300 to 500 K. Atmospheric opacities were obtained from the measurement of the sky emissivity and the use of the ATM code (Cernicharo 1985; Pardo et al. 2001), and found to be between 0.1 and 0.2 corresponding to 1 to 3 mm of precipitable water vapor. Focus and pointing were checked every 3 hours and 1.5–2 hours respectively on intense nearby sources. The map is centered at the position of the infrared source IRc2 ( $\alpha=05^{\text{h}}35^{\text{m}}14.5^{\text{s}}$ ,  $\delta=-05^{\text{d}}22^{\text{m}}29.3^{\text{s}}$  /  $\alpha=83.81037^\circ$ ,  $\delta=-05.3748^\circ$ ). The reference position which is free of CO emission was located at an offset ( $-3600''$ ,  $-1800''$ ).

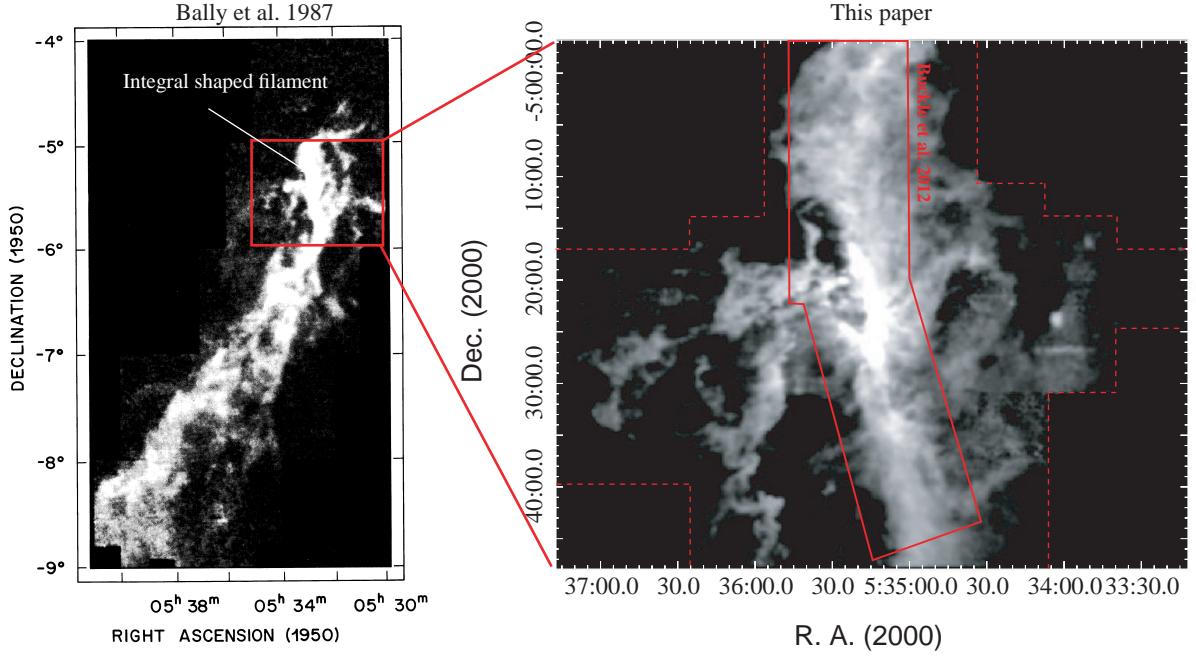


Fig. 1.— *Left:* Map of the  $^{13}\text{CO}$  (1-0) integrated intensity of the Orion A complex presented in Bally et al. (1987) with an angular resolution of  $1'$ . *Right:* Map of the  $^{13}\text{CO}$  (2-1) integrated intensity (see Fig. 3 for details) obtained with the IRAM 30m telescope, with a maximal resolution of  $11''$ , presented in this article. The limits of the mapped region are indicated with the red dashed line. The polygon with continuous red borders indicates the region mapped in the CO (3-2) line by Buckle et al. (2012). Both maps are shown as gradations of gray scale intensities (see Fig. 3 for absolute scale).

Data reduction was performed using the GILDAS software<sup>2</sup>. Several corrections were applied to the data: one of the problems concerns the combination of submaps obtained over different observing sessions with different intensity calibration, weather conditions and pointing errors. Position switching observations (PSW) were performed at the position of IRc2 before each OTF submap and these were used afterwards to correct for such differences between submaps. Relative errors in pointing corrections were obtained comparing these PSW observations with the 4'' spacing <sup>12</sup>CO map observed within the 2 × 2 line survey (see Esplugues et al. 2013 and Marcelino et al., in prep). We have found pointing errors between submaps typically of 2–4'', with a few cases of large errors of 7–10'' in RA under poor weather conditions. Besides the pointing errors in the observations, we found that pixels in the array are not perfectly aligned. We obtained a measurement of pixel misalignment in both HERA1 and HERA2 arrays, using <sup>12</sup>CO and <sup>13</sup>CO maps of IRC+10216 (Cernicharo et al., in preparation). The errors found are between 0.1 – 2''. Further corrections on the intensity calibration were needed in order to account for the different response of each pixel within the HERA array. The different calibration between pixels is due to the fact that the image band rejection cannot be measured for each individual receiver in the array. Since this parameter will depend on the tuning, maps performed in different days will show different intensity calibration. Therefore, the data were scaled using a factor which depends on the particular submap and pixel in the array. This factor was obtained comparing the emission in each pixel with respect to the central one in the array, which was found to be the most uniform over the whole map. After all these corrections were applied, the final map was constructed using a pixel size of 5.5'' i.e. half the beam size. The total number of positions in the map are 99415 after reduction, each with an on-source integration time of 10 seconds (~1 sec. at the most external parts of the map) corresponding with rms of ~0.2

---

<sup>2</sup><http://www.iram.fr/IRAMFR/GILDAS>

K (0.4–0.5 K at the map borders).

### 3. Results

Figures 2 and 3 show the  $^{12}\text{CO}$  and  $^{13}\text{CO}$   $J = 2 - 1$  integrated emission maps between  $-5$  to  $25 \text{ km s}^{-1}$ . While  $^{12}\text{CO}$  shows a widespread emission across the observed region, the less abundant and optically thin isotopomer  $^{13}\text{CO}$ , delineates the densest regions, showing a very clumpy and filamentary structure. The bulk of the gas is mainly distributed along the ISF (Bally et al. 1987), clearly delineated by the densest gas seen in  $^{13}\text{CO}$  emission (Fig. 3). This filament contains the Orion Molecular Clouds 1–4 (see below). The gas distribution extends East and West of the main filament, but not equally. Whilst emission spreads continuously to the East and southeast, showing numerous clumps and filaments, it is truncated sharply Southwest to the filament, coincident with a region where X-ray emission is observed (Güdel et al. 2008). Further West of this empty region where no CO emission was found, a spherical clump and an elongated cloud (E-W) are observed. These features, are only seen at blue shifted velocities (see below), suggesting that they are being pushed toward the observed by a bubble of hot and ionised gas from massive stars. Indeed the elongated cloud is composed of several clumps (or “ripples”) whose geometry and velocity suggest they are the result of a Kelvin-Helmholtz instability produced by the expansion of the nebula (Berné et al. 2010).

The Orion Molecular Cloud 1 (OMC-1), located behind the Orion Nebula, is the brightest region seen at the center of the filament and contains well-known features such as the BN/KL infrared nebula, the Orion-South region (Ori-S) and the Bar, which positions are indicated in Fig. 2.

In contrast to the bright emission of the Bar, the KL nebula and Ori-S, there is a small



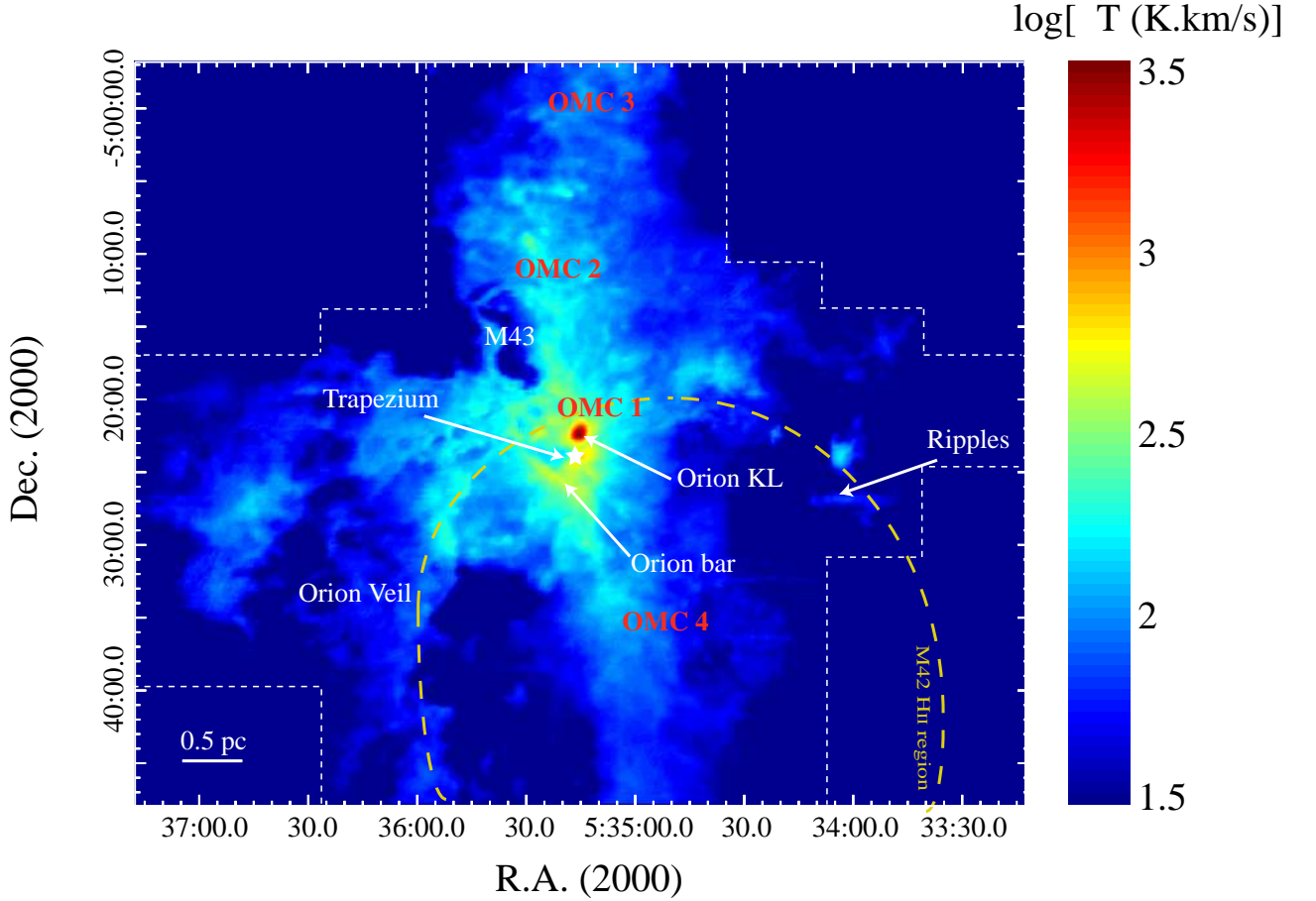


Fig. 2.— IRAM 30m maps of the decimal logarithm of velocity integrated  $^{12}\text{CO}$  (2-1) emission of the Orion molecular cloud. Distinctive objects within the Nebula are indicated. The yellow dashed line indicates the approximate limits of the HII region M42, based on the thermal Bremsstrahlung (free-free) emission observed at 330 MHz by (Subrahmanyan et al. 2001), while the white dashed line indicates the limits of the field of view. See [http://userpages.irap.omp.eu/~oberne/Olivier\\_Berne/Data](http://userpages.irap.omp.eu/~oberne/Olivier_Berne/Data) for larger resolution versions of this image and data in FITS format.

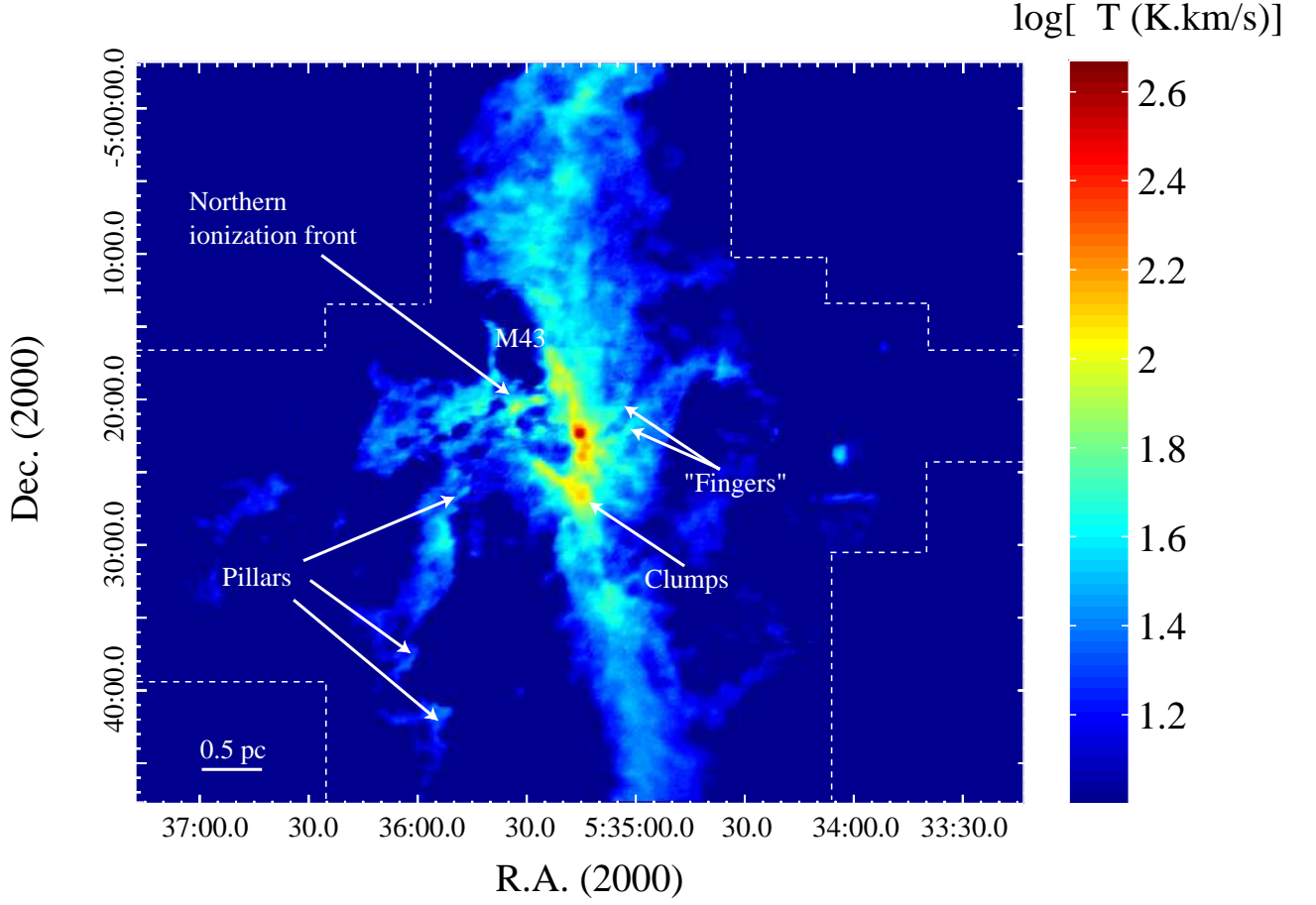


Fig. 3.— IRAM 30m maps of the decimal logarithm of velocity integrated  $^{13}\text{CO}$  (2-1) emission of the Orion molecular cloud. Distinctive objects within the Nebula are indicated. See [http://userpages.irap.omp.eu/~oberne/Olivier\\_Berne/Data](http://userpages.irap.omp.eu/~oberne/Olivier_Berne/Data) for larger resolution versions of this image and data in FITS format.

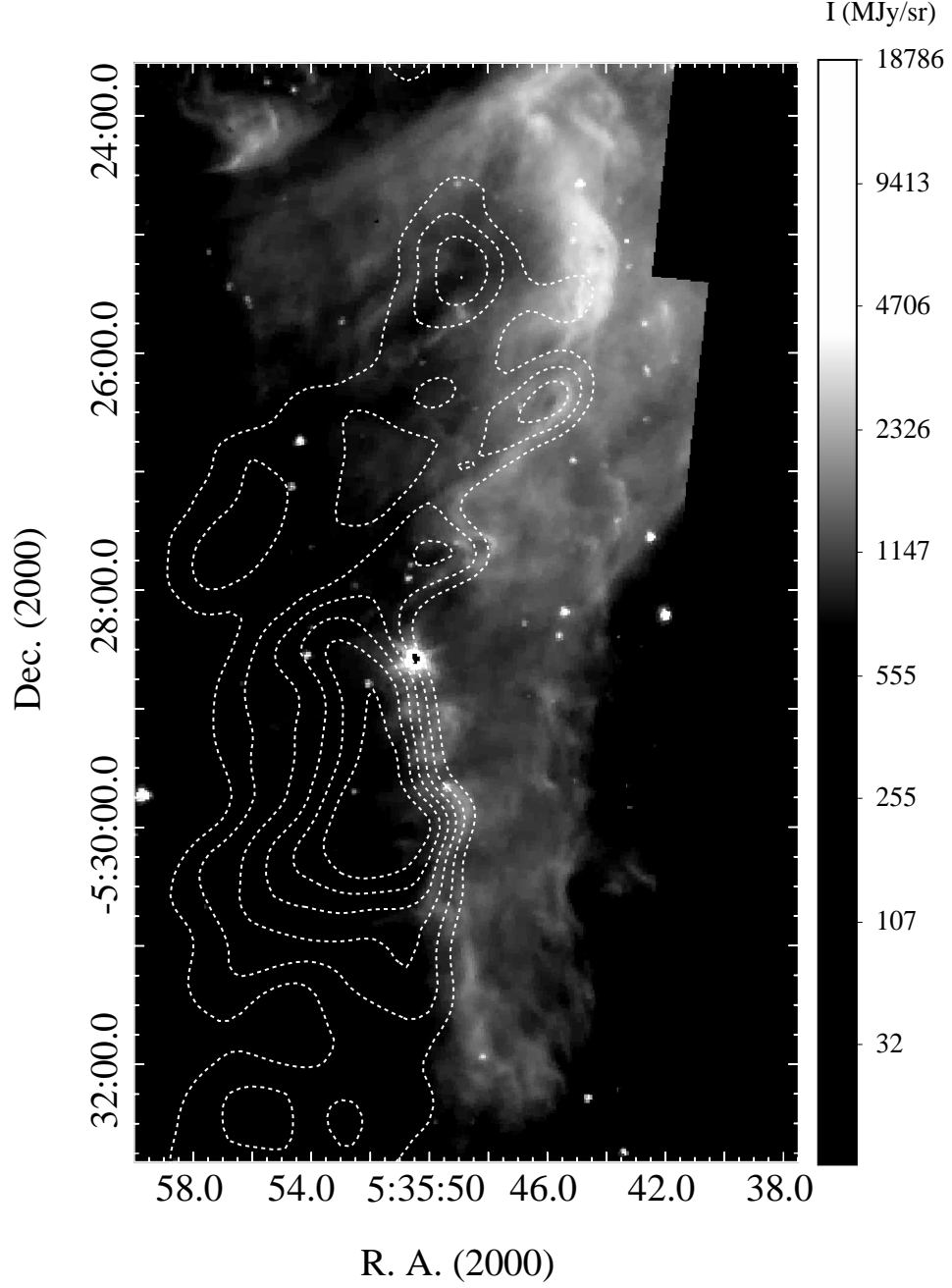


Fig. 4.— Map of the *Spitzer*-IRAC 3.6  $\mu\text{m}$  emission due to PAHs in the region of the pillars (grayscale). The dashed contours show the velocity integrated  $^{13}\text{CO}$  (2-1) intensity. Contours start at 20 K.km.s $^{-1}$  and increase in steps of 4 K.km.s $^{-1}$ .

region of weak emission which corresponds to the position of the Trapezium stars. This region is limited by the M42 HII region ionization fronts (the Northern Ionization Front and the Bar to the south), and by the molecular ridge to the West. It is easy to see, in the  $^{12}\text{CO}$  maps, the close relation of these bright features with the cone-like ionized structure of M42 observed in radio-continuum emission (Yusef-Zadeh 1990). The North Ionization Front (NIF) is formed by several filaments running southwest-southeast (see  $^{13}\text{CO}$  emission in Fig. 3). The NIF is the counterpart of the obscured filament seen in the optical images of the Orion Nebula and known as the “Dark Lane”. Further East, other clumps appear which follow the same direction as the NIF, indicating they might be related. In  $^{12}\text{CO}$  (Fig. 2), low density gas East to the NIF is observed. This emission ends abruptly in a wall-like structure from which few thin filaments or streamers spread towards East, like tunnels blowing the molecular gas to the clumps seen at the eastern most part of the map. South to the NIF a filamentary structure going nearly North-South is seen (Fig. 3), which should also be related to the expansion of the HII region (see Rodriguez-Franco et al. 1998). Cometary shaped pillars are well visible in this region (Fig. 3). The fact that these are pointing towards the Trapezium stars strongly suggest that these structures are the result of the selective photo-erosion of the Nebula, following the model proposed by Reipurth (1983). This is illustrated in more details in Fig. 4 where we overlay the  $^{13}\text{CO}$  emission and the *Spitzer*-IRAC 3.6  $\mu\text{m}$  image in this particular region. While  $^{13}\text{CO}$  traces the inner molecular cloud, the IRAC image is thought to trace the emission from UV heated polycyclic aromatic hydrocarbons (PAHs), present in the mostly atomic gas at the surface of the molecular cloud. It is clear from Fig. 4 that the PAH emission enshrouds the molecular pillars and peaks systematically closer to the Trapezium stars as compared to CO. This stratification is classical in photon-dominated regions (PDRs, see for instance Tielens et al. (1993) for a classical example in the Orion Bar) and hence also favors the idea that selective photo-erosion is at the origin of these Pillars. Immediately to the

West of Orion-KL, elongated structures or *Fingers* (Rodriguez-Franco et al. 1992) are detected. These structures are believed to be the result of the interaction of the molecular cloud with the extreme environment (especially the flow of ionized gas, see discussion in Rodriguez-Franco et al. 1992).

The northern part of the ISF shows strong  $^{12}\text{CO}$  emission (Fig. 2), which is separated in several clumps in the  $^{13}\text{CO}$  map (see Fig. 3). This region correspond to the molecular clouds OMC-2 and OMC-3. Both regions are known to be very active in star formation since many young protostars and pre-main sequence stars have been detected in the infrared and submillimeter wavelengths, together with molecular outflows and jets (see Peterson & Megeath 2008, for a review). Indeed, the turbulent  $^{12}\text{CO}$  emission in OMC-2/3 indicates the presence of such outflows (see section 4.3). The  $^{13}\text{CO}$  emission on the other hand, is very clumpy (Fig. 3), showing the densest cores where star formation is taking place. To the southeast of OMC-2, there is a cavity empty of molecular emission, clearly seen in the  $^{13}\text{CO}$  map (Fig. 3) which corresponds to the HII region M43. This cavity, which in the optical is nearly spherical, is a small HII region illuminated by the B0.5 star  $\nu$  Ori (Thum et al. 1978). M43 is limited in molecular emission by the ISF to the west, and a thin filament to the east that connects OMC-2 to the NIF. To the South, the ISF seems less clumpy and active in star formation than the northern filament (e.g. no outflow signatures observed). There is a local maximum located about  $700''$  south of Orion-KL, corresponding to the OMC-4 molecular cloud. This molecular core was identified in the CO maps of Loren (1979) and in the SCUBA 450 and  $850\ \mu\text{m}$  emission observed by Johnstone & Bally (1999). In their submillimeter maps, this cloud is seen as a bright concentration of knots in a V-shaped structure.

## 4. Analysis

### 4.1. Column density map

#### 4.1.1. Method

Assuming local thermodynamic equilibrium and optically thin emission (which is mostly the case for  $^{13}\text{CO}$ ), the  $^{13}\text{CO}$  column density can be obtained using an excitation temperature derived from the peak temperature of the  $^{12}\text{CO}$  line (see, e.g. Goldsmith & Langer 1999). The  $^{13}\text{CO}$  column density can be converted into a column density  $N(H_2)$  using the abundance ratio  $[H_2]/[^{13}\text{CO}] = 7 \times 10^5$ . Of course, the derivation of column density in this manner is limited by the assumptions made, in particular  $^{13}\text{CO}$  may become moderately optically thick in some regions of the Nebula with high column densities (see e.g. Castets et al. 1990). In dense and cold regions, CO is also expected to be depleted on grains and the  $[H_2]/[^{13}\text{CO}]$  ratio may become larger than the one used. Both of these effects will imply an underestimation of the total column density of the order of a few for dense regions. In the rest of the nebula we expect our estimation to be relatively robust. We have computed  $N_H$  on each pixel of the map (Fig. 5). Column densities derived in this way range between a few times  $10^{18}$  and a few times  $10^{23} \text{ cm}^{-2}$ . We have mapped the points which correspond to column densities below  $3 \times 10^{21} \text{ cm}^{-2}$ , corresponding to the typical visual extinction at which CO can survive (e.g. Draine 2011). We found that these points correspond to noisy  $^{13}\text{CO}$  spectra i.e. with a peak brightness below 0.6 K, i.e. 3 times the typical sensitivity of  $\sim 0.2$  K per channel, where the column density cannot be evaluated with confidence. Therefore we have thresholded our map at  $3 \times 10^{21} \text{ cm}^{-2}$  (Fig. 5). We also define arbitrarily three subregions in the map presented in Fig. 5: the North region, which contains OMC-2/3 and corresponds to the regions where many low mass stars are present, the South region, which contains OMC4, the ripples and the cometary shaped

pillars and corresponds to the parts of the cloud which enshroud the M42 HII region, and finally, the central region, corresponding to the the most active and complex parts of the nebula, in which Orion-KL, the Bar, the molecular Fingers and the NIF are found.

#### 4.1.2. *General properties*

The map of column density derived from the  $^{13}\text{CO}$  data is shown in Fig.5. Moderate column densities of a few times  $10^{21-22}\text{cm}^{-2}$  are found along the ISF. The column density for the Orion-KL is of the order of  $5\times 10^{23}\text{cm}^{-2}$  (Fig. 5) close to the values reported recently by Plume et al. (2012). Fig. 6 presents a close-up view of the column density map in the Orion Bar region. The Bar has a typical maximum column density of  $10^{23}\text{cm}^{-2}$ . This map suggests the presence of clumpy structures, and we have identified 4 specific clumps. They correspond well in position (Table 1) and shape to the clumps seen in the  $^{13}\text{CO}$  (3-2) and  $\text{C}^{18}\text{O}$  (3-2) maps of Buckle et al. (2012) (see their Fig. 7). The good match between the positions of these clumps in  $^{13}\text{CO}$  (2-1),  $^{13}\text{CO}$  (3-2) and  $\text{C}^{18}\text{O}$  (3-2) indicates that the emission in these transition is only moderately affected by optical depth effects in the Bar. We note that these clumps appear relatively large (diameter  $> 14''$ , see Table 1) and therefore differ from the arcsecond scale clumps proposed to exist by van der Werf et al. (1996) and Goicoechea et al. (2011). In the case these mini-clumps also exist in the Bar, this would suggest that clumpy structures with different spatial scales coexist. The maximum column densities for these clumps are 9, 10, 11, and  $13 \times 10^{22}\text{cm}^{-2}$  for clumps number 4, 3, 2, and 1 respectively. These values are comparable with the column densities derived for the Orion bar based on far infrared dust emission by Arab et al. (2012). Apart from the ISF and classical structures described above, other notables structures are found with significant column densities: the ripples ( a few times  $10^{21}\text{cm}^{-2}$  ), the clump just North of the ripples ( a few times  $10^{22}\text{cm}^{-2}$ ) as well as the

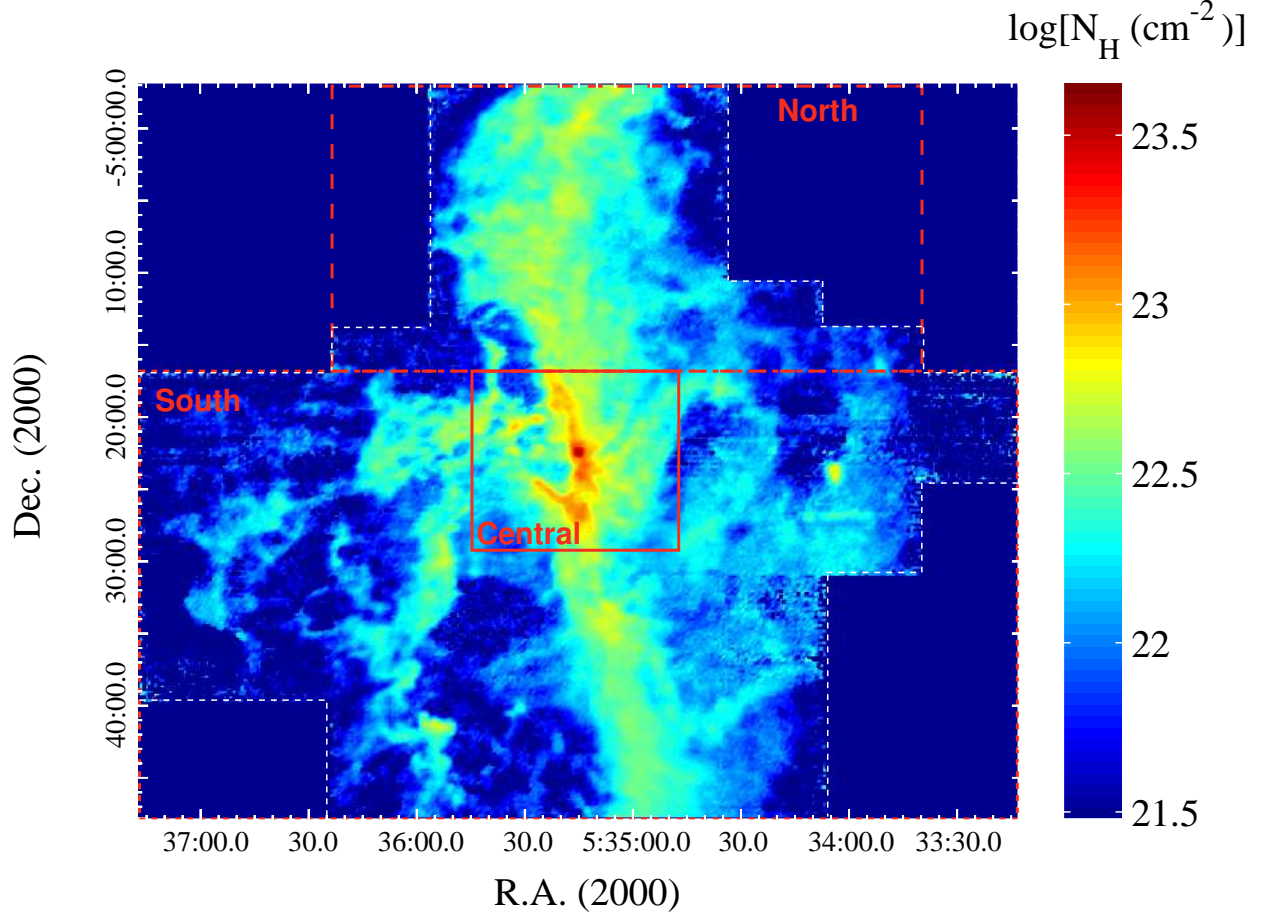


Fig. 5.— Map of the decimal logarithm of column density  $N_H$  in the Orion molecular cloud estimated from the  $^{12}\text{CO}(2-1)$  and  $^{13}\text{CO}(2-1)$  data (see text for details). The threshold for this map is  $N_H = 3 \times 10^{21} \text{ cm}^{-2}$  corresponding to typical optical depths above which CO is expected to survive to photodissociation. The borders of the sub-regions mentioned in the text and in Table 2 are indicated with the red dashed boxes. See [http://userpages.irap.omp.eu/~oberne/Olivier\\_Berne/Data](http://userpages.irap.omp.eu/~oberne/Olivier_Berne/Data) for larger resolution versions of this image and data in FITS format.



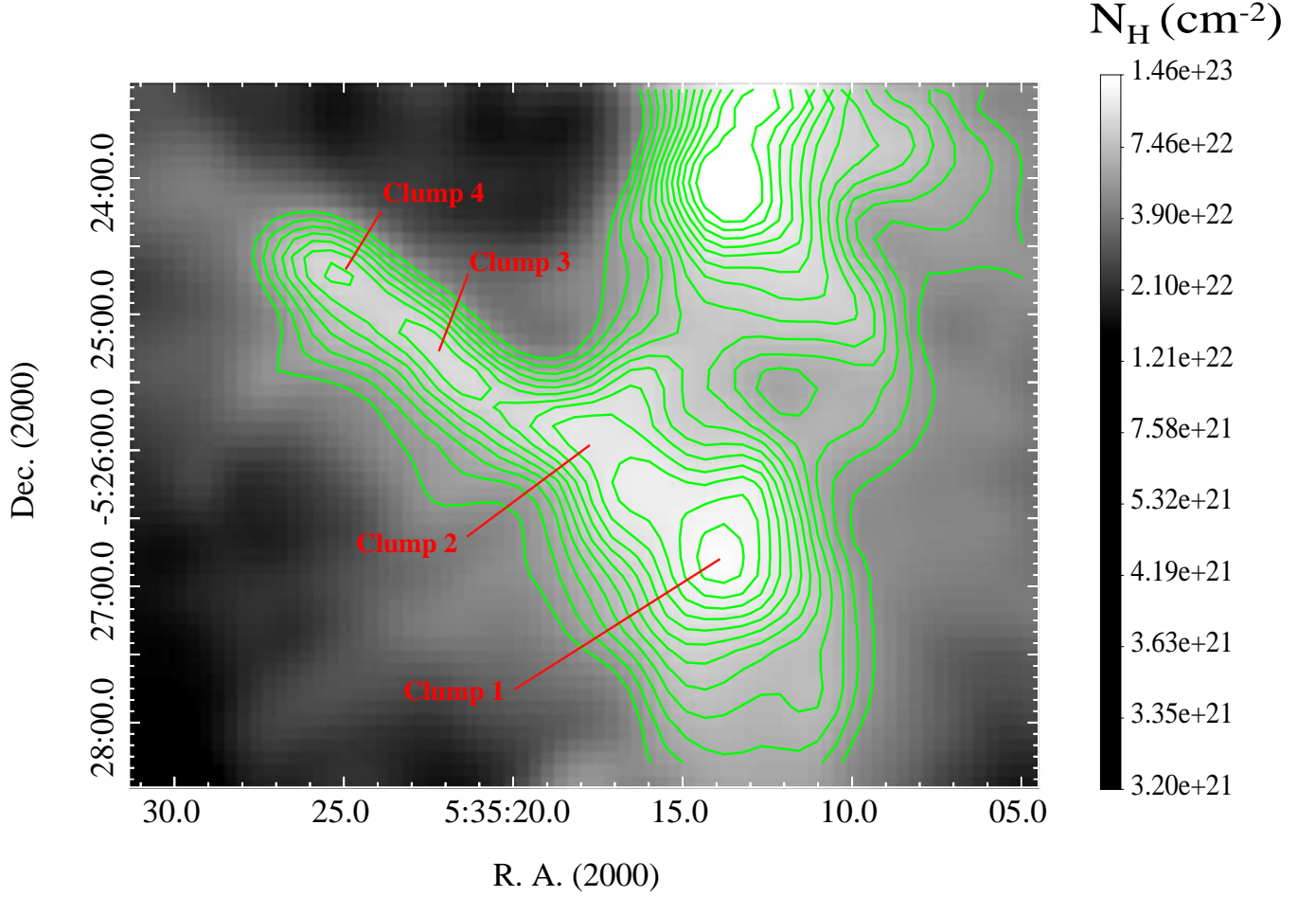


Fig. 6.— Column density map of the Orion bar region (greyscale). The contours start at  $5 \times 10^{22} \text{ cm}^{-2}$  and increase by steps of  $2/3 \times 10^{22} \text{ cm}^{-2}$  up to  $1.3 \times 10^{23} \text{ cm}^{-2}$ . The four clumps identified in the Bar are indicated.

wall of pillars at the edge the the Veil in the South-East. The molecular fingers also appear with high column densities ( $10^{22-23}\text{cm}^{-2}$ ). The readers interested in the details of the structure of these regions can find the fits file image of the column density map at [http://userpages.irap.omp.eu/~oberne/Olivier\\_Berne/Data.html](http://userpages.irap.omp.eu/~oberne/Olivier_Berne/Data.html)

## 4.2. Mass

We can derive the total mass of the cloud using:

$$M = \mu m_H \int_S N(H_2) dS \quad (1)$$

where  $\mu = 2.8$  is the mean molecular weight and  $m_H$  is the atomic hydrogen mass. This integral is calculated on each pixel of the column density map, using the map pixel size ( $5'' \times 5''$  at 414 pc) as the unit of surface. The total mass is then derived by summing all the integrals. Using this approach, we find a total mass of  $\sim 7700 M_\odot$ , close to the value derived by Castets et al. (1990) using  $^{13}\text{CO}$  (1-0) for a similar field of view. We computed the the mass of the integral shaped filament, using Eq. 1 but considering the field of view of Buckle et al. (2012) (see Fig. 1). This field is centered on Orion KL and follows the brightest emission of the ISF. With this field of view, we find a mass of  $4300 M_\odot$ , in excellent agreement with the mass of  $4290 M_\odot$  derived by Buckle et al. (2012) using  $^{13}\text{CO}$  (3-2) but smaller than the value reported by Bally et al. (1987) of  $5000 M_\odot$ . Considering that these latter authors used a distance of 500 pc (instead of 414 pc here) and a mean molecular weight of 2.6 (while we use a value of 2.8) to estimate the mass of the ISF, their value could be overestimated by a factor  $(2.6 \times 500^2)/(2.8 \times 414^2) = 1.35$  as compared to ours. On the other hand, in their computation, Bally et al. (1987) consider a North-to-South extent of about  $1.5^\circ$  for the ISF, compared to  $0.85^\circ$  in our case. Overall, we conclude that the mass we derive for the ISF is in very good agreement with the value of Buckle et al. (2012), where a direct comparison is possible. As compared the value of Bally et al. (1987) the

agreement is reasonable considering the uncertainty in the area used to derive the mass. Since the total mass we derive for the cloud is about  $7700 M_{\odot}$ , dense molecular gas present in the ISF actually represents only about half of the cloud mass. Hence, a large fraction of the cloud mass reside in more diffuse extended filamentary structures. Using the column density map, we have estimated that most of this mass in the *diffuse* molecular gas lies in regions of column densities lower than  $3 \times 10^{22} \text{ cm}^{-2}$ , or at a visual extinction  $A_V$  below 10. The diffuse and filamentary molecular gas in these regions can be observed thanks to the high sensitivity obtained with the 30m telescope. These results stress the importance of sensitive surveys in order to calculate accurate masses of molecular gas in nearby and extragalactic environments. Using the same method as above, we derive the masses of the clumps identified in the Orion Bar (see Fig 6). We have assumed a circular geometry with radii given in Table 1. The masses are found to range between 4.3 and 52 Solar masses (Table 1). Condensations with similar masses are often observed around HII regions (see e.g. Deharveng et al. 2009), and it is believed that they result from the compression of the molecular cloud due to the expansion of the ionized bubble.

### 4.3. Kinematics

#### 4.3.1. Subtraction of the North-South velocity gradient

As mentioned in Bally et al. (1987) (see their Fig. 5), the Orion A cloud is subject to a velocity gradient over a scale of about 25 pc from North to South. This is also visible at the smaller scale which we study here and was reported as well in Buckle et al. (2012) (see their Fig. 3 for a position-velocity diagram illustrating this effect). When trying to study the small scale fluctuations of the velocity field, it is therefore useful to subtract this velocity gradient. Hence, both our  $^{12}\text{CO}$  and  $^{13}\text{CO}$  spectral cubes are corrected from a  $0.7 \text{ km s}^{-1} \text{ pc}^{-1}$  velocity gradient. This gives spectral cubes which are in the rest frame of

the ISF, and can be used to study spatially the fluctuations of the velocity field without contamination from the large scale *falling backwards* effect. For these two cubes, we redefine  $v = 0$  at the peak of the line obtained by averaging the cube over the spatial dimensions.

#### 4.3.2. Kinematics from $^{12}\text{CO}$

$^{12}\text{CO}$  has the advantage to be bright but on the other hand this line quickly becomes optically thick. Hence, it is useful to study detailed spatial structures corresponding to emission in the optically thin high velocity wings of this line. This is particularly suited for the study of outflows and jets emanating from protostars. Using the velocity gradient subtracted cube of  $^{12}\text{CO}$ , we compute two maps corresponding to the emission in the high velocity wings of this line. The “blue” map (corresponding to blue shifted velocities in the frame of the ISF) is obtained by integrating the cube in velocity between  $[-\infty, -4.8]$   $\text{km s}^{-1}$ . The “red” map instead is obtained by integrating over the  $[+3.2, \infty]$   $\text{km s}^{-1}$  range. In Fig. 7, we present an overlay of the “blue” and “red” maps. In the South region, OMC-4 appears blue-shifted, mostly likely because it sits in front of the HII region, and is pushed towards the observer. To the east of OMC-4 is an arc shaped structure is clearly visible. This structure had been identified by Loren (1979) and most likely represents the back of the cloud situated behind the HII region. The difference between the mean velocity of the blue and red shifted parts of the cloud in the South region is of the order of  $\Delta v \sim 10 \text{ km s}^{-1}$ . With a radius of 1.8 pc for the HII region, this implies a –short– dynamical age of about  $t_{\text{dyn}} \sim 0.2$  Myrs for the expansion of the Nebula due to the growth of the HII region. The ripples also appear in blue, and hence seem to be part of a foreground cloud as was already proposed by Berné et al. (2010). In the North region,  $^{12}\text{CO}$  looks more mixed/turbulent due to red and blue emission most likely arising due to the intense star formation and hence outflow activity in this region (e.g. Chini et al. 1997; Aso et al. 2000; Williams et al. 2003).

In Fig. 8, we overlay the red and blue maps of  $^{12}\text{CO}$  to the MIPS  $24\mu\text{m}$  image obtained by *Spitzer*, focusing on the Northern region of the nebula only. In addition, we indicate the positions of the far infrared clumpy structures that can be identified (by eye) in the SCUBA  $850\mu\text{m}$  map obtained by Johnstone & Bally (1999). It clearly appears that numerous elongated blue/red shifted structures find their origin at positions of  $24\mu\text{m}$  sources and/or FIR clumps, which are both indicators of the positions of young stellar objects. We do not study these structures individually since this has been done in great details by Aso et al. (2000) and Williams et al. (2003). Nevertheless, Fig. 8 suggests that most of the red and blue shifted structures seen in Fig. 8 correspond to protostellar outflows, and that the dynamical properties of the nebula in this region are likely to be affected, or perhaps dominated (Williams et al. 2003), by this activity.

#### 4.3.3. Kinematics from $^{13}\text{CO}$

As opposed to  $^{12}\text{CO}$ ,  $^{13}\text{CO}$  has the advantage to be more optically thin but less bright. Hence, it is useful tracer to study the inner structure of the molecular gas. Using the velocity gradient subtracted cube of  $^{13}\text{CO}$ , we compute two maps corresponding to the emission in the blue and redshifted sides of the line. i.e. the “blue” map is obtained by integrating the cube in velocity between  $[-\infty, 0]$   $\text{km s}^{-1}$  and the “red” map instead is obtained by integrating over the  $[0, \infty]$   $\text{km s}^{-1}$  range. In Fig. 9, we present an overlay of the corresponding “blue” and “red” maps. Following the ISF from Orion KL, towards the North or the South, the filament successively appears in red and then blue, with a periodicity of the order of about  $20'$ . This pattern is compatible with a helical filament, which could be due to the structure of the large scale magnetic field which has been suggested to be helical (see Uchida et al. 1991; Matthews et al. 2001; Poidevin et al. 2011; Buckle et al. 2012). Whether this structure is at the origin of the formation of Orion KL (e.g. by the Parker

instability as suggested by Shibata & Matsumoto 1991) or resulting from the formation of Orion KL (e.g. acting as a drain of angular momentum as suggested by Uchida et al. 1991) is unclear and should be investigated in more details. In any case, this suggests that the magnetic field plays a dominant role in the evolution of the cloud. The comparative study between the kinematics of the cloud and the magnetic field combining the present CO data with the large -scale polarization data from the Planck satellite will be particularly useful to investigate this subject.

#### 4.4. Energy balance

Using the  $^{13}\text{CO}$  map we compute a map of the full width at half maximum (FWHM) of the lines and write this parameter  $\delta v$ . From this, we can derive a map of the turbulent kinetic energy in the gas defined by  $E_k = 1/2M \times \delta v^2$ , with  $M$  as defined in Eq. 1. The total kinetic energy of the cloud is  $E_k = 3.6 \times 10^{40}$  J. This value is slightly higher than the kinetic energy derived by Buckle et al. (2012) of  $2.53 \times 10^{40}$  J, but, as for the mass, this is probably because the field of view studied in the present paper is larger. In the central region, Orion KL contains  $\sim 1.1 \times 10^{39}$  J of kinetic energy in the molecular gas. This number is one order of magnitude smaller than that derived by Peng et al. (2012). However, these authors consider the difference between the median velocity in the blue and red wings of the CO (6-5) line to measure velocity dispersion. Therefore their number is not directly comparable to the one derived here. The Orion Bar contains  $\sim 2.3 \times 10^{39}$  J, and the molecular fingers  $\sim 3.7 \times 10^{39}$  J. The rest of the kinetic energy in the central region is distributed in various filamentary structures, for instance in the Northern ionization front filament. The North region holds about  $8.9 \times 10^{39}$  J, a value comparable to the kinetic energy derived by Williams et al. (2003) using CO (1-0) observations of  $7.4 \times 10^{39}$  J, for the same region, and attributed to outflows.

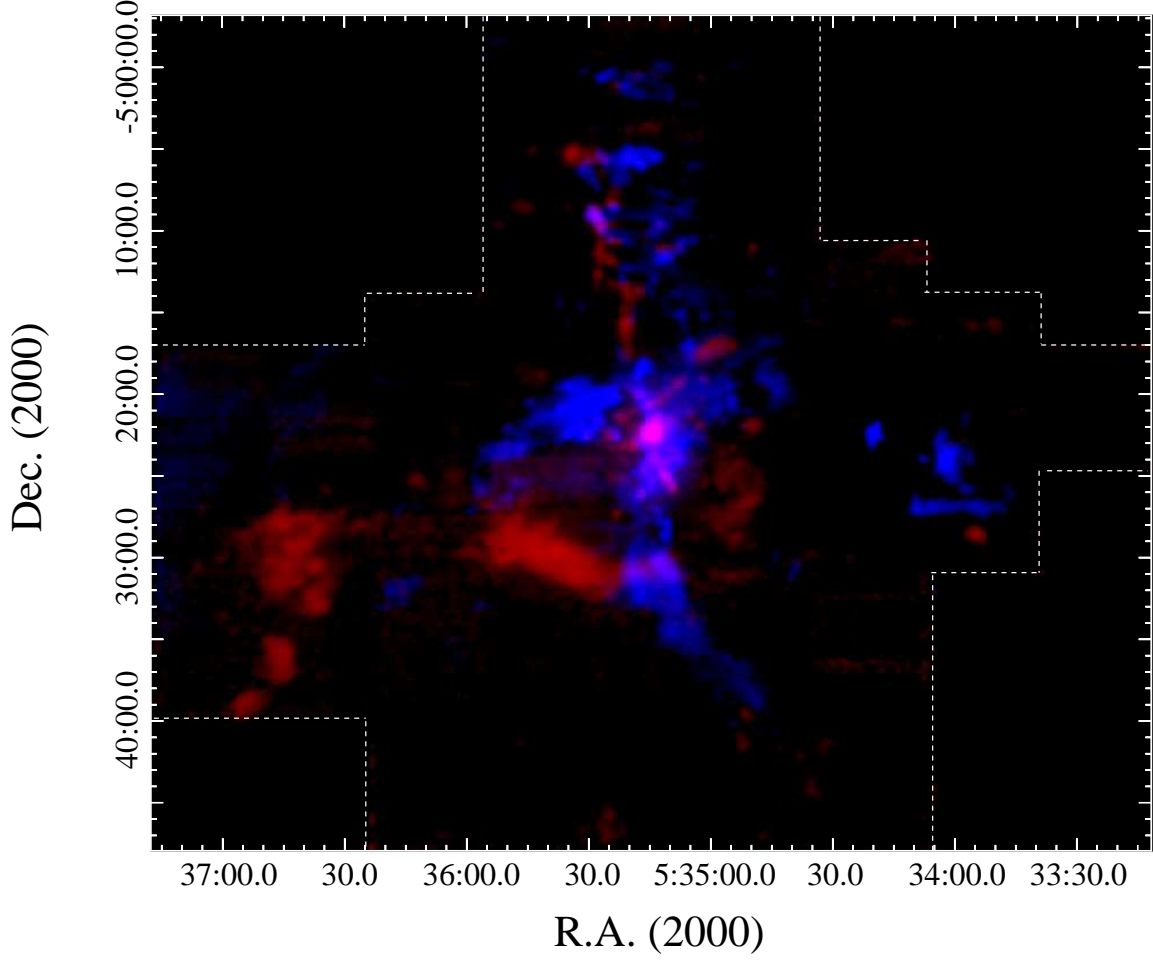


Fig. 7.— Velocity integrated emission in the wings of the  $^{12}\text{CO}$  emission line, after subtraction of the North-South velocity gradient to the spectral cube. Blue corresponds to velocities in the range  $[-\infty, -4.8]$   $\text{km s}^{-1}$  and red to velocities in the range  $[+3.2, \infty]$   $\text{km s}^{-1}$ , where the zero velocity correspond to the core velocity of the cloud (see text for details).

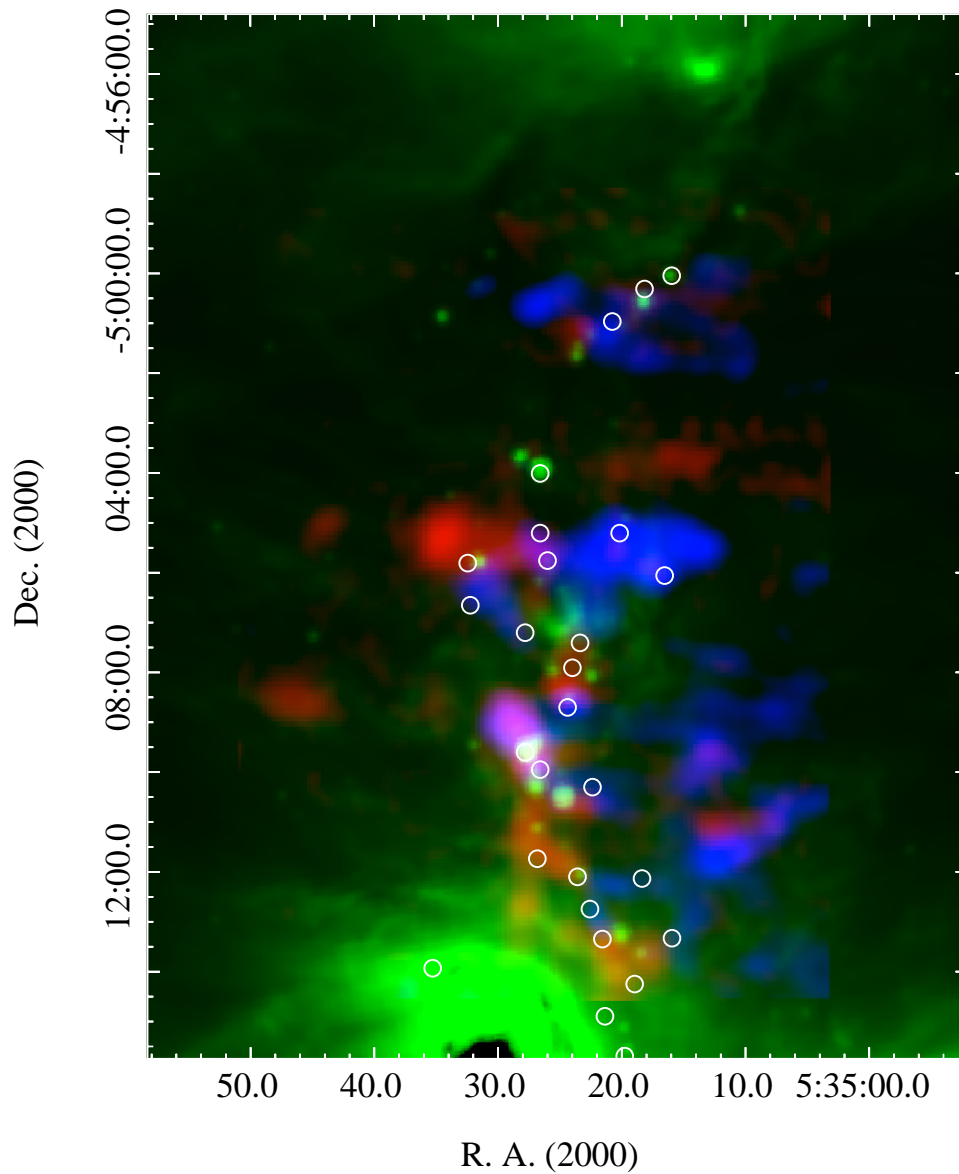


Fig. 8.— Northern region of the nebula, showing the red and blue components of the  $^{12}\text{CO}$  emission (same as those of Fig.7) as well as the *Spitzer*-MIPS 24  $\mu\text{m}$  map in green. The far infrared clumps identified in the SCUBA 850  $\mu\text{m}$  map of Johnstone & Bally (1999) are indicated by the white circles.



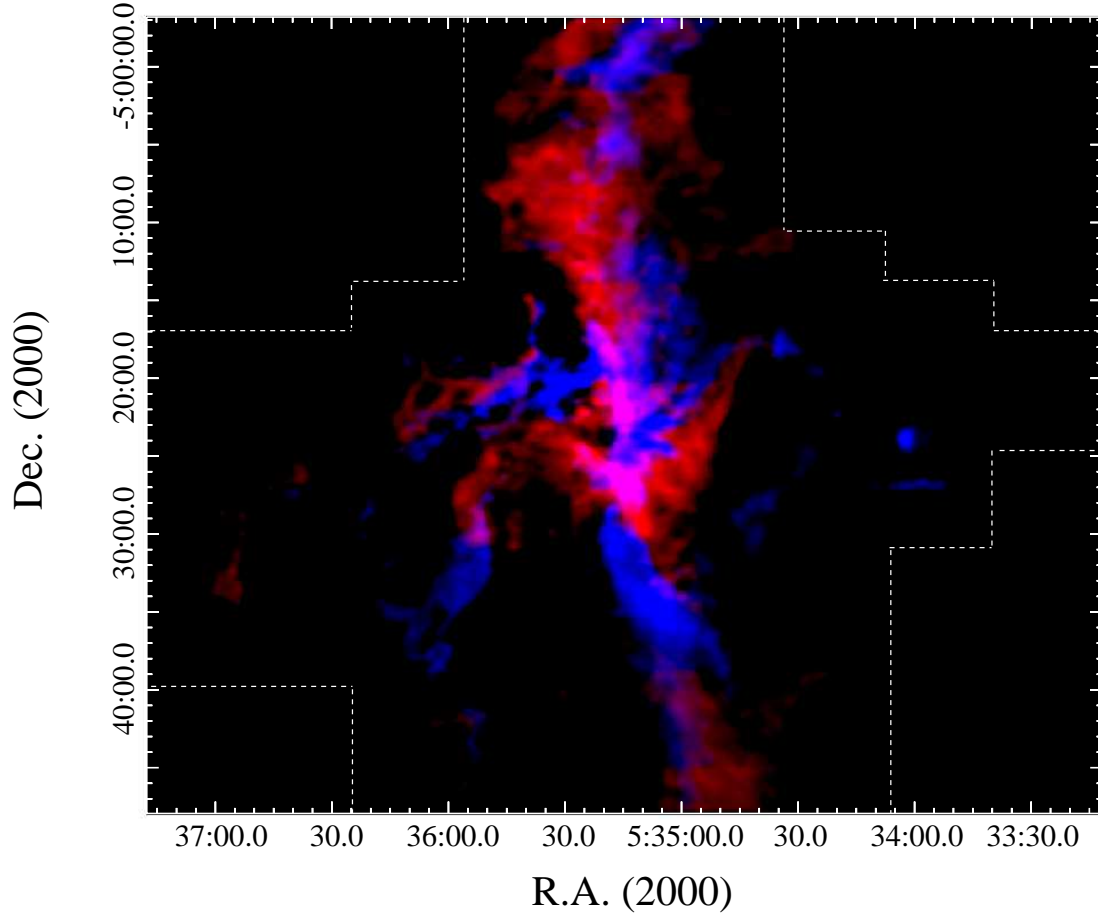


Fig. 9.— Velocity integrated emission in the  $^{13}\text{CO}$  emission line, after subtraction of the North-South velocity gradient to the spectral cube. Blue corresponds to velocities in the range  $[-\infty, 0]$   $\text{km s}^{-1}$  and red to velocities in the range  $[0, +\infty]$   $\text{km s}^{-1}$ , where the zero velocity correspond to the core velocity of the cloud (see text for details).

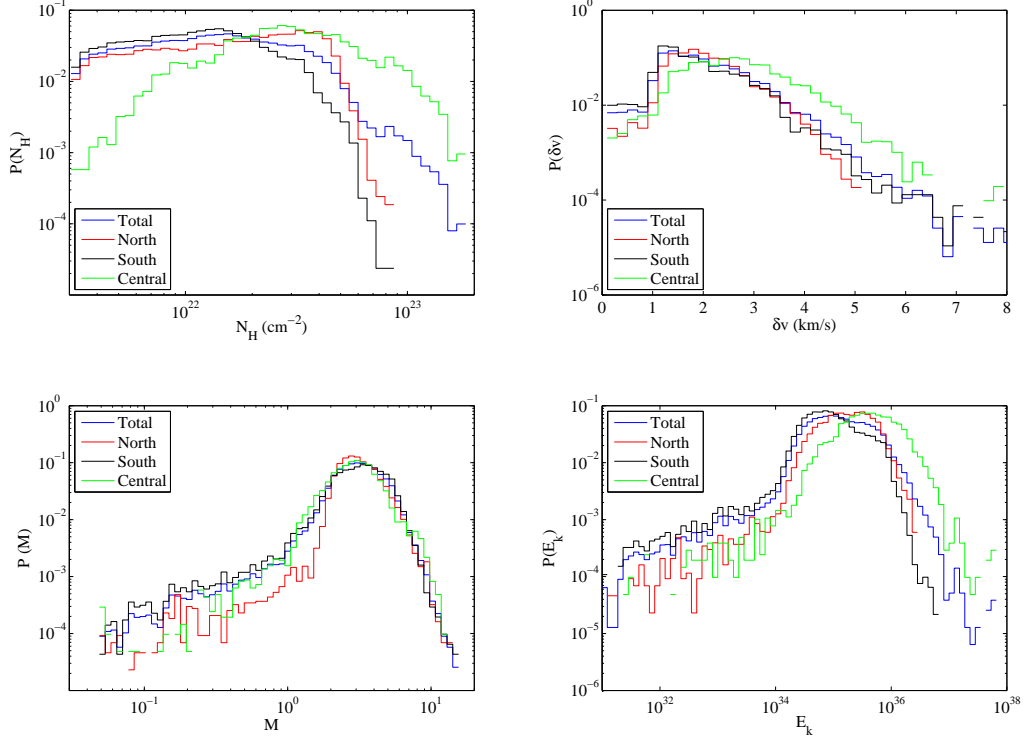


Fig. 10.— Probability density functions of the per-pixel column density  $N_H$ , turbulent velocity dispersion  $\delta v$ , Mach number  $\mathcal{M}$ , and kinetic energy  $E_k$

Assuming that most of the mass of the nebula lies in the ISF, and adopting a cylindrical geometry, we can calculate the gravitational energy by  $E_p = 2GM^2/3R$  with  $R$  the radius of the cylinder. The CO images suggest a value of  $R = 0.2^\circ = 4.2 \times 10^{16}$  m. This yields a gravitational energy  $E_p = 2.5 \times 10^{41}$  Joules, larger than the kinetic energy of the cloud. The thermal energy of the Orion molecular cloud,  $E_t = (3/2)k_B TM/\mu m_H = 3.4 \times 10^{39}$  J, is an order of magnitude smaller than the gravitational potential, adopting a temperature of 50 K for the molecular gas (the molecular gas would need to be 500 K for the thermal energy to be comparable to the gravitational energy, which is unrealistic). The intensity of the magnetic field in the Orion Nebula has been measured by Brogan et al. (2005) and Abel et al. (2004) and found to vary between 5 and 25 nT. Adopting once more a cylindrical geometry, we can estimate magnetic energy by  $E_B = Rh^2B/8$ , where  $h$  is the North-to-South extent of the nebula (measured to be  $h = 1.9 \times 10^{17}$  m) and  $B$  the magnetic field strength. For the above mentioned values of  $B$ , we find a range of magnetic energy  $E_B = 2 - 10 \times 10^{41}$  J.

In summary, the magnetic energy is comparable, or larger, than the gravitational potential and an order of magnitude larger than the kinetic energy. The thermal energy in the molecular cloud is negligible compared to these numbers.

Now focusing on the Orion bar region, we consider the equilibrium for the four clumps seen in the Orion bar (Fig. 6). For these four clumps, we derive the mean velocity dispersion  $\langle \delta v \rangle$ , from the map velocity dispersion  $\delta v$  and inside a circular aperture with position and radii given in Table 2. The values of  $\langle \delta v \rangle$  for each clump are given in Table 2. Using the values reported in Table 2 for mass, radius and velocity dispersion, we can derive the virial parameter defined as (e.g. Bertoldi & McKee 1992)  $\alpha = 5 \langle \delta v \rangle^2 \times R_{clump}/GM_{clump}$  for each clump.

We find that all the  $\alpha$  values are large (Table 2), indicating that these clumps are

subcritical and are confined by the external pressure or are evaporating. Using the physical size (Table 2), column densities (Fig. 6) and a typical gas temperature of 30-50 K yields pressures of the order of a few  $10^6 \text{ K.cm}^{-3}$  for these clumps. Assuming a magnetic field strength of the same order of magnitude as that derived by Abel et al. (2004) (5-25 nT i.e. 50-250  $\mu\text{G}$ ) yields magnetic pressure also of the order of a few  $10^6 \text{ K.cm}^{-3}$  for the ambient medium. Since the magnetic field is expected to increase inside the clump where the density is higher, it will be acting to support the clump against collapse. Thus the cloud must be evaporating, unless the ambient thermal pressure is greater than a few  $10^6 \text{ K.cm}^{-3}$ . The results of Abel et al. (2004) indicate that the latter is not the case and hence these clumps are probably evaporating. Assuming evaporation at the sound speed yields mass loss rates lower than a few  $10^{-7} \text{ M}_\odot/\text{year}$ , and these clumps will therefore live for timescales larger than that of the nebula.

Overall, this suggest that the magnetic field plays a major role in supporting the integral shaped filament (Bally et al. 1987; Fiege & Pudritz 2000; Buckle et al. 2012) as well a small scale structures such as clumps.

#### 4.5. Probability density functions

We derive the probability density functions (PDF) of the column density  $N_H$ , turbulent velocity dispersion  $\delta v$ , and kinetic energy  $E_k$ . In addition, we derive the PDF of the turbulent Mach number  $\mathcal{M}$ , given by the ratio  $\delta v/c_s$ , where  $c_s$  is the sound speed.  $c_s$  is derived assuming the that the gas temperature is equal to the excitation temperature derived from the  $^{12}\text{CO}$  line. For each one of these parameters, we compute the PDF for the whole region, but also for the 3 sub-regions identified in Fig. 5. The resulting PDFs are presented in Fig. 10.

The column density PDF is found to be non-Gaussian and relatively flat. Column density histograms in star-forming regions are known to exhibit power-law tails (see for instance recent examples in Kainulainen et al. 2011). In our case the combination of a gaussian and a power law gives poor fits to the observed histogram. A collection of power laws can give a reasonably good fit, but this is at the expense of many arbitrary choices such as the number of power laws used. It is interesting to note that similarly flat column density PDFs have been produced by MHD simulations of the turbulent saturation of the Kelvin-Helmholtz instability (Hendrix & Keppens 2014), which has been proposed as a source of small scale turbulence in the Orion molecular cloud by Berné & Matsumoto (2012). When comparing the PDFs of the three sub-regions, it clearly appears that the central regions hosts the largest column densities, present in the Orion Bar and Orion-KL. The North region also appears to have higher column densities than the more diffuse South region. The North region shows a sharp decrease at a column density of  $N_H \sim 4 \times 10^{22} \text{ cm}^{-2}$ , perhaps corresponding to the limit of gravitational stability. Both the higher column density and presence of this sharp edge are consistent with the fact that the North region is much more active in terms of star-formation than the South region.

The PDFs of the velocity dispersion show a peak between 1 and 2 km/s, typical for molecular clouds and a log linear tail towards larger velocities. The North and South regions show very similar  $\delta v$  PDFs, while the PDF of the central region is shifted towards larger velocities due to the intense kinetic activity of Orion-KL. The PDFs of the Mach number peak around 2-3, indicating that turbulence is highly supersonic in Orion. The PDF of the North region appears sharper than in the central and South region, and peaks at a lower Mach number. This particularity is likely the result of the low-mass star-formation activity i.e. linked to the fact that turbulence in this region is dominated by the outflow activity.

Finally, the last panel of Fig. 10 shows the distribution of the kinetic energy. Logically,

the central region contains the pixels with highest kinetic energies, due to the presence of Orion KL. The North region also displays higher kinetic energies than the South region. This is most likely because of the intense outflow activity in the North region, which is an efficient source of kinetic energy.

#### 4.6. Distribution of the feedback processes

The distribution of the kinetic energy as well as other sources of energy are summarized in Table 2. In order to estimate the contribution from different feedback processes we classify the regions and their corresponding kinetic energies either in the “outflow-driven” or “HII region-driven” feedback categories. The kinetic energy in the Orion bar is most likely the result of the expansion of the HII region and there is very little outflow activity there. On the contrary, Orion-KL is most likely dominated by outflows, jets, or explosive motions, which all result from the feedback of massive protostars so we classify it in the outflow-driven feedback category. Following Rodríguez-Franco et al. (1992) we consider that the kinetic energy in the molecular fingers results from the interaction of the molecular cloud with the HII region. The situation is less clear for the various filamentary structures seen in the central region. The contribution of both the HII region and outflow may be present so we consider that half of the feedback originates from outflows and the other half from the HII region. In the South region which is directly in contact with the expanding HII region, and where large scale blue and red-shifted structures are seen, most of the kinetic energy results from the feedback of the HII region. However there is known outflow activity in OMC-4, with a kinetic energy of  $1.35 \times 10^{39}$  J (Rodríguez-Franco et al. 1999). In the North, as suggested by Fig. 8 and in Sect. 4.5, the dynamical energy most likely originates for a large part from outflows of low mass protostars (see also Williams et al. 2003) so we classify this region in the outflow category. All in all we find that the kinetic

energy resulting from outflow activity  $E_{OF}$  represents  $1.5 \times 10^{40}$  J while the kinetic energy due to interaction with the HII region  $E_i$  represents  $2.1 \times 10^{40}$  J. This implies that 40% of the kinetic energy injected in the cloud is provided by outflows and 60% by the interaction with the HII region.

#### 4.7. Fraction of radiated energy converted into kinetic energy

$E_i$  can be compared to the radiative energy injected in terms of ionizing photons by  $\theta^1 C$ . Assuming that most of its luminosity lies in ionizing photons and using  $L_* = 2.1 \times 10^5 L_\odot$ , we find  $E_* = L_* \times t_{dyn} \sim 5 \times 10^{44}$  Joules. Most of this energy is transferred to the HII region (Ferland 2001) in the form of thermal, kinetic and magnetic energy. With  $E_i = 2.1 \times 10^{40}$ , this implies that less than  $\sim 0.01\%$  of the energy injected in starlight has been transferred in the molecular cloud in the form of kinetic energy. This value is naturally small, because most of the energy of the HII region is radiated away. An additional fraction of kinetic energy may be present in the HII region (photo-evaporation flows, champagne flows see e.g. Ochsendorf et al. 2014) but this has not been evaluated observationally so far. Assuming a total lifetime for  $\theta^1 C$  of  $\sim 3$  Myrs and a constant injection efficiency implies that, in total, a few times  $10^{41}$  Joules of kinetic energy will be injected in the ISM due to the evolving HII region. This is at least one order of magnitude smaller than what can be injected by a supernova explosion (Thornton et al. 1998), but is distributed over a much longer timescales, and may thus have a profound impact on the evolution of the galactic ecosystem and on triggered star formation.

#### 4.8. On triggered star formation in Orion

Triggered star-formation theories stipulate that the formation of a massive star and the following expansion of an HII region can compress and fragment the surrounding molecular cloud, resulting in the formation of a subsequent generation of low-mass stars. This process has been convincingly identified to be at play in the molecular shells around a number of bubble shaped HII regions (see e.g. Deharveng et al. 2010b for a recent overview). Here on the other hand, we find that the molecular cloud directly in contact with the HII region in the South (OMC4, the Veil) shows lower column densities than the Northern region (OMC 2-3). Such conditions disfavor star-formation, and indeed the South region shows very few signs of star-forming activity although Shimajiri et al. (2011) have identified a few sub regions where star-formation could occur. Clearly, the North region contains much more protostars than the South region, and this suggest that the triggered star-formation due to the HII region is not effective in Orion. Given the young dynamical age we have derived (0.2 Myr), it is possible that triggering will occur later. Alternatively, an explanation could be that triggered star formation at the edge of expanding HII regions is only favored around well confined HII bubbles. Here in Orion, instead, the HII region may not be well confined and a champagne flow could be releasing the pressure, especially through a cavity towards the Eridanis super-bubble in the South-East (Güdel et al. 2008). In this case, the Orion HII region would already be in blister phase, and therefore the pressure driven expansion of the HII region is expected to be much reduced, as well as the compression of the surrounding cloud and the triggering of star-formation.

### 5. Summary and conclusions

We presented new large scale maps of the Orion molecular cloud in the  $^{12}\text{CO}$  and  $^{13}\text{CO}$  (2-1) lines. The nebula appears filamentary and turbulent. Using this dataset we derive the



following parameters: a dynamical age for the nebula  $t_{dyn} \sim 0.2$  Myrs, a total mass of the nebula  $M = 7700M_{\odot}$ . About half of this mass resides in the dense integral shaped filament at the center of the nebula while the other half resides in more diffuse and filamentary structures distributed around the filament. We find a total kinetic energy  $E_k = 3.6 \times 10^{40}$  J for the cloud, about 40% of which emanates from the outflows and the rest from feedback of the HII region. However, the relative importance of the feedback processes depends on the considered sub-regions within the cloud. The North region of the cloud, (OMC-2/3) seems dominated by feedbacks from outflows. In the central region (OMC-1), the feedback is shared between the protostellar outflows and feedback from the HII region. The South region, instead, seems dominated by the feedback due to the expansion of the HII region. Overall, it seems that the feedback from the HII region, which is often invoked as the most important source in the triggering of star-formation is not exceeding by a large number the feedback due to outflows, and therefore both mechanisms may be important. In addition, we find that the triggering of star-formation by the expansion of the HII region seems inefficient in Orion. We find that only about  $\sim 0.01\%$  of the energy radiated by  $\theta^1C$  has been converted into kinetic energy in the molecular cloud. Over the lifetime of this star, a few  $10^{41}$  Joules may be injected in the ISM. This is much smaller than what can be injected by a supernova but can still have a significant influence on the shaping of the ISM and the regulation of star-formation, since this occurs on larger timescales. Finally, we suggest that magnetic fields probably have an important role in the energy balance, at small and large scales. We propose that the integral shaped filament has a helical shape, perhaps following the magnetic field lines, and is rotating about its main axis.

We acknowledge the two referees of this paper who helped improving the manuscript. We thank Paul Goldsmith for his comments. The National Radio Astronomy Observatory is a facility of the National Science Foundation operated under cooperative agreement by

Associated Universities, Inc.

Table 1: Properties of the clumps in the Orion bar

Name	Position	Radius	Mass	Velocity dispersion	Virial paramater
Name	(R. A., Dec.) (deg.)	$R_{clump}$ (")	$M_{clump}$ ( $M_{\odot}$ )	$\delta V$ (km/s)	$\alpha$
Clump 1	(83.8075, -5.44827)	46.3	52.1	3.03	18.9
Clump 2	(83.8192, -5.43942)	23.4	13.6	2.08	17.3
Clump 3	(83.8431, -5.42102)	23.8	11.3	2.11	21.8
Clump 4	(83.8559, -5.41123)	14.7	4.30	2.12	35.6

Table 2: Derived parameters for the Orion molecular cloud

General parameters	
Total mass $M$	$7700 M_{\odot}$
Expansional velocity $\Delta V$	$10 \text{ km s}^{-1}$
Dynamical age $\tau_{dyn}$	$0.2 \text{ Myrs}$
Energy (Joules)	
Turbulent kinetic energy $E_k$	$3.6 \times 10^{40}$
South region (OMC-4)	$1.3 \times 10^{40}$
North region (OMC 2-3)	$8.9 \times 10^{39}$
Central region (OMC 1)	$1.4 \times 10^{40}$
... Orion bar	$2.3 \times 10^{39}$
... Orion KL	$1.1 \times 10^{39}$
... Molecular fingers	$3.7 \times 10^{39}$
... Filamentary structures in the central region	$6.5 \times 10^{39}$
Gravitational energy $E_p$	$2.5 \times 10^{41}$
Thermal energy $E_t$	$3.4 \times 10^{39}$
Magnetic energy $E_B$	$2 - 10 \times 10^{41}$
Starlight $E_*$	$5 \times 10^{44}$

## REFERENCES

- Abel, N. P., Brogan, C. L., Ferland, G. J., O’Dell, C. R., Shaw, G., & Troland, T. H. 2004, *ApJ*, 609, 247
- Arab, H., Abergel, A., Habart, E., Bernard-Salas, J., Ayasso, H., Dassas, K., Martin, P. G., & White, G. J. 2012, *A&A*, 541, A19
- Aso, Y., Tatematsu, K., Sekimoto, Y., Nakano, T., Umemoto, T., Koyama, K., & Yamamoto, S. 2000, *ApJS*, 131, 465
- Bachiller, R. 1996, *ARA&A*, 34, 111
- Bally, J. Overview of the Orion Complex, ed. B. Reipurth, 459
- Bally, J., Lanber, W. D., Stark, A. A., & Wilson, R. W. 1987, *ApJ*, 312, L45
- Berné, O., Marcelino, N., & Cernicharo, J. 2010, *Nature*, 466, 947
- Berné, O. & Matsumoto, Y. 2012, *ApJ*, 761, L4
- Bertoldi, F. & McKee, C. F. 1992, *ApJ*, 395, 140
- Brogan, C. L., Troland, T. H., Abel, N. P., Goss, W. M., & Crutcher, R. M. 2005, in *Astronomical Society of the Pacific Conference Series*, Vol. 343, *Astronomical Polarimetry: Current Status and Future Directions*, ed. A. Adamson, C. Aspin, C. Davis, & T. Fujiyoshi, 183
- Buckle, J. V., Davis, C. J., Francesco, J. D., Graves, S. F., Nutter, D., Richer, J. S., Roberts, J. F., Ward-Thompson, D., White, G. J., Brunt, C., Butner, H. M., Cavanagh, B., Chrysostomou, A., Curtis, E. I., Duarte-Cabral, A., Etxaluze, M., Fich, M., Friberg, P., Friesen, R., Fuller, G. A., Greaves, J. S., Hatchell, J., Hogerheijde, M. R., Johnstone, D., Matthews, B., Matthews, H., Rawlings, J. M. C., Sadavoy, S.,

- Simpson, R. J., Tothill, N. F. H., Tsamis, Y. G., Viti, S., Wouterloot, J. G. A., & Yates, J. 2012, MNRAS, 422, 521
- Castets, A., Duvert, G., Dutrey, A., Bally, J., Langer, W. D., & Wilson, R. W. 1990, A&A, 234, 469
- Cernicharo, J. 1985, IRAM report number 52
- Chini, R., Reipurth, B., Ward-Thompson, D., Bally, J., Nyman, L.-A., Sievers, A., & Billawala, Y. 1997, ApJ, 474, L135
- Deharveng, L., Schuller, F., Anderson, L. D., Zavagno, A., Wyrowski, F., Menten, K. M., Bronfman, L., Testi, L., Walmsley, C. M., & Wienen, M. 2010a, A&A, 523, A6
- . 2010b, A&A, 523, A6
- Deharveng, L., Zavagno, A., Schuller, F., Caplan, J., Pomarès, M., & De Breuck, C. 2009, A&A, 496, 177
- Draine, B. T. 2011, Physics of the Interstellar and Intergalactic Medium
- Dutrey, A., Duvert, G., Castets, A., Langer, W. D., Bally, J., & Wilson, R. W. 1991, A&A, 247, L9
- Elmegreen, B. G. 1998, in Astronomical Society of the Pacific Conference Series, Vol. 148, Origins, ed. C. E. Woodward, J. M. Shull, & H. A. Thronson, Jr., 150
- Elmegreen, B. G. & Scalo, J. 2004, ARA&A, 42, 211
- Esplugues, G. B., Tercero, B., Cernicharo, J., Goicoechea, J. R., Palau, A., Marcelino, N., & Bell, T. A. 2013, A&A, 556, A143
- Ferland, G. J. 2001, PASP, 113, 41

- Fiege, J. D. & Pudritz, R. E. 2000, *ApJ*, 534, 291
- Frieman, E. A. 1954, *ApJ*, 120, 18
- Genzel, R. & Stutzki, J. 1989, *ARA&A*, 27, 41
- Goicoechea, J. R., Joblin, C., Contursi, A., Berné, O., Cernicharo, J., Gerin, M., Le Bourlot, J., Bergin, E. A., Bell, T. A., & Röllig, M. 2011, *A&A*, 530, L16
- Goldsmith, P. F. & Langer, W. D. 1999, *ApJ*, 517, 209
- Güdel, M., Briggs, K. R., Montmerle, T., Audard, M., Rebull, L., & Skinner, S. L. 2008, *Science*, 319, 309
- Hendrix, T. & Keppens, R. 2014, *A&A*, 562, A114
- Johnstone, D. & Bally, J. 1999, *ApJ*, 510, L49
- Kainulainen, J., Beuther, H., Banerjee, R., Federrath, C., & Henning, T. 2011, *A&A*, 530, A64
- Loren, R. B. 1979, *ApJ*, 234, L207
- Matthews, B. C., Wilson, C. D., & Fiege, J. D. 2001, *ApJ*, 562, 400
- Megeath, S. T., Gutermuth, R., Muzerolle, J., Kryukova, E., Flaherty, K., Hora, J. L., Allen, L. E., Hartmann, L., Myers, P. C., Pipher, J. L., Stauffer, J., Young, E. T., & Fazio, G. G. 2012, *AJ*, 144, 192
- Menten, K. M., Reid, M. J., Forbrich, J., & Brunthaler, A. 2007, *A&A*, 474, 515
- Muench, A., Getman, K., Hillenbrand, L., & Preibisch, T. 2008, in *Handbook of Star Forming Regions, Volume I*, ed. B. Reipurth, 483

- Ochsendorf, B. B., Verdolini, S., Cox, N. L. J., Berné, O., Kaper, L., & Tielens, A. G. G. M. 2014, ArXiv e-prints
- Pardo, J., Cernicharo, J., & Serabyn, E. 2001, *Antennas and Propagation, IEEE Transactions on*, 49, 1683
- Peng, T.-C., Zapata, L. A., Wyrowski, F., Güsten, R., & Menten, K. M. 2012, *A&A*, 544, L19
- Peterson, D. E. & Megeath, S. T. The Orion Molecular Cloud 2/3 and NGC 1977 Regions, ed. B. Reipurth, 590
- Plume, R., Bergin, E. A., Phillips, T. G., Lis, D. C., Wang, S., Crockett, N. R., Caux, E., Comito, C., Goldsmith, P. F., & Schilke, P. 2012, *ApJ*, 744, 28
- Poidevin, F., Bastien, P., & Jones, T. J. 2011, *ApJ*, 741, 112
- Reipurth, B. 1983, *A&A*, 117, 183
- Rodriguez-Franco, A., Martin-Pintado, J., & Fuente, A. 1998, *A&A*, 329, 1097
- Rodriguez-Franco, A., Martin-Pintado, J., Gomez-Gonzalez, J., & Planesas, P. 1992, *A&A*, 264, 592
- Rodríguez-Franco, A., Martín-Pintado, J., & Wilson, T. L. 1999, *A&A*, 351, 1103
- Roy, J.-R. & Kunth, D. 1995, *A&A*, 294, 432
- Shibata, K. & Matsumoto, R. 1991, *Nature*, 353, 633
- Shimajiri, Y., Kawabe, R., Takakuwa, S., Saito, M., Tsukagoshi, T., Momose, M., Ikeda, N., Akiyama, E., Austermann, J. E., Ezawa, H., Fukue, K., Hiramatsu, M., Hughes, D., Kitamura, Y., Kohno, K., Kurono, Y., Scott, K. S., Wilson, G. W., Yoshida, A., & Yun, M. S. 2011, *PASJ*, 63, 105



- Spitzer, Jr., L. 1954, *ApJ*, 120, 1
- Subrahmanyam, R., Goss, W. M., & Malin, D. F. 2001, *AJ*, 121, 399
- Thornton, K., Gaudlitz, M., Janka, H.-T., & Steinmetz, M. 1998, *ApJ*, 500, 95
- Thum, C., Lemke, D., Fahrback, U., & Frey, A. 1978, *A&A*, 65, 207
- Tielens, A. G. G. M., Meixner, M. M., van der Werf, P. P., Bregman, J., Tauber, J. A., Stutzki, J., & Rank, D. 1993, *Science*, 262, 86
- Uchida, Y., Fukui, Y., Minoshima, Y., Mizuno, A., & Iwata, T. 1991, *Nature*, 349, 140
- van der Werf, P. P., Goss, W. M., & O’Dell, C. R. 2013, *ApJ*, 762, 101
- van der Werf, P. P., Stutzki, J., Sternberg, A., & Krabbe, A. 1996, *A&A*, 313, 633
- Williams, J. P., Plambeck, R. L., & Heyer, M. H. 2003, *ApJ*, 591, 1025